Annals of Biomedical Engineering (© 2014)
DOI: 10.1007/s10439-014-0973-0

BMES BIOMEDICAL ENGINEERING SOCIETY™ www.bmes.org

Architectural Trends in the Human Normal and Bicuspid Aortic Valve Leaflet and Its Relevance to Valve Disease

ANKUSH AGGARWAL,[1] GIOVANNI FERRARI,[2] ERIN JOYCE,[3] MICHAEL J. DANIELS,[4] RACHANA SAINGER,[2] JOSEPH H. GORMAN III,[2] ROBERT GORMAN,[2] and MICHAEL S. SACKS[1]

[1]Center for Cardiovascular Simulation, Institute for Computational Engineering Sciences and the Department of Biomedical Engineering, The University of Texas at Austin, 201 East 24th Street, ACES 5.438, One University Station, C0200, Austin, TX 78712-0027, USA; [2]Gorman Cardiovascular Research Group, University of Pennsylvania, Philadelphia, PA, USA; [3]Department of Bioengineering, University of Pittsburgh, Pittsburgh, PA, USA; and [4]Division of Statistics & Scientific Computation and Department of Integrative Biology, University of Texas at Austin, Austin, TX, USA

(*Received 30 September 2013; accepted 9 January 2014*)

Associate Editor Jane Grande-Allen oversaw the review of this article.

Abstract—The bicuspid aortic valve (AV) is the most common cardiac congenital anomaly and has been found to be a significant risk factor for developing calcific AV disease. However, the mechanisms of disease development remain unclear. In this study we quantified the structure of human normal and bicuspid leaflets in the early disease stage. From these individual leaflet maps average fiber structure maps were generated using a novel spline based technique. Interestingly, we found statistically different and consistent regional structures between the normal and bicuspid valves. The regularity in the observed microstructure was a surprising finding, especially for the pathological BAV leaflets and is an essential cornerstone of any predictive mathematical models of valve disease. In contrast, we determined that isolated valve interstitial cells from BAV leaflets show the same *in vitro* calcification pathways as those from the normal AV leaflets. This result suggests the VICs are not intrinsically different when isolated, and that external features, such as abnormal microstructure and altered flow may be the primary contributors in the accelerated calcification experienced by BAV patients.

Keywords—Microstructure, Aortic stenosis, Calcific aortic valve disease, Early disease stage, Fiber structure, Valve interstitial cells.

NOMENCLATURE

AV	Aortic valve
TAV	Tricuspid aortic valve
BAV	Bicuspid aortic valve
AS	Aortic stenosis
AVSc	Aortic valve sclerosis
CAVD	Calcific aortic valve disease
VIC	Valve interstitial cell
AVA	Aortic valve area
ECM	Extra cellular matrix
SALS	Small angle light scattering
H&E	Hematoxylin and Eosin
MMP	Modified Movat Pentachrome
DMEM	Dulbecco's modified Eagle's medium
SMA	Smooth muscle actin
GAPDH	Glyceraldehyde 3-phosphate dehydrogenase
RMSD	Root mean square distance
MRI	Magnetic resonance imaging
OI	Orientation index

Address correspondence to Michael S. Sacks, Center for Cardiovascular Simulation, Institute for Computational Engineering Sciences and the Department of Biomedical Engineering, The University of Texas at Austin, 201 East 24th Street, ACES 5.438, One University Station, C0200, Austin, TX 78712-0027, USA. Electronic mail: msacks@ices.utexas.edu

INTRODUCTION

The aortic heart valve (AV) normally consists of three cuspal shaped leaflets (''tricuspid,'' or TAV) that regulate blood flow from left ventricle to the aorta. However, there exist congenital anomalies wherein two of the leaflets are fused to form a bicuspid aortic valve (BAV). BAV defects occur in about 1–2% of the population, making it the most prevalent congenital cardiac anomaly. Growing clinical and scientific data indicate that BAV is an exceptionally strong risk factor for life threatening aortic valve and/or ascending aortic

Published online: 01 February 2014

pathology.[6,8,11,24] Accelerated valve calcification producing aortic stenosis (AS) before the sixth decade of life is the most common clinical manifestation of BAV. Previous studies have indicated that the biological mechanism of calcium deposition in BAV patients is similar to the calcification process that occurs in patients with a TAV; however the process is greatly accelerated for reasons that are not clearly understood. It should be noted that BAV is part of a larger spectrum of AV structural anomalies that range from single to quad leaflet forms.[5,16,17,23]

Progression of calcific aortic valve disease (CAVD) starts with asymptomatic stages that include mild thickening of the leaflets without affecting valvular function—a condition called aortic valve sclerosis (AVSc). In some cases, AVSc progresses to severe calcification, loss of leaflet mobility and symptomatic AS. At the microstructural level, CAVD is characterized by extensive remodeling of the cusps with biomineralization of the fibrosa layer as valve interstitial cells (VICs) adopt an osteogenic like phenotype.[4] Once osteogenic nodules form, epitaxial deposition of amorphous calcium phosphate can occur without cell mediated regulation.[28] The early identification of patients who are at the greatest risk of developing AS would be of great clinical value.[28]

Overall, little quantitative knowledge is available about the structural differences between the TAV and BAV at different length scales, especially regards to population based trends, and how these differences might contribute to accelerated calcification. Past research efforts have aimed at understanding the structural BAV anomaly and its effect on heart valve disease have been primarily focused on genetics,[9] along with blood hemodynamics and flow patterns resulting in altered shear stresses being seen as contributors to the CAVD pathogenesis.[2] The latter has been supported by recent evidence in *ex vivo* studies that altered wall shear stresses do not change the leaflet structure and cell viability but promote fibrosa endothelial activation.[26] While these studies suggest a relation to BAV disease development, the exact pathways in which the endothelial cells communicate with the interstitial cells remains to be determined. Moreover, these factors may not be the entire story about the onset and progression of the disease process. We speculate that, in addition to current identified pathways, tissue and organ structural features unique to the BAV also contribute to the onset and progression of CAVD. However, tissue structural features of the BAV, especially the presence of any consistent trends, are currently unknown.

Based on these considerations, we compared the structural properties of human explanted pre-diseased bicuspid and normal aortic valve leaflets at the cellular, tissue, and organ levels. We analyzed explanted AV tissues to obtain their microstructural properties using several techniques, and developed a novel spline technique to develop population-based average valve architectures. We discuss the role of current findings in the accelerated development of CAVD among BAV patients and their potential use in prediction of the onset of calcification.

MATERIALS AND METHODS

Human Sample Collection

After approval by University of Pennsylvania Institutional Review Board human aortic valve tissue was obtained at the time of cardiac surgery. The presence of a BAV or TAV morphology was confirmed by preoperative transesophageal echocardiology and direct inspection. Calcified valve leaflets were obtained from the patients undergoing aortic valve replacement. Non-calcified tissues (i.e., from patients with non-calcified healthy valves) were obtained from hearts excised at the time of heart transplantation or from donor hearts that were not used for transplantation. Patients were grouped as TAV (non calcified and calcified) and BAV (non calcified and calcified), and demographical information of the patients recorded (Table 1).

TABLE 1. Patient demographics.

	TAV		BAV		
	Non calcified	Calcified	Non calcified	Calcified	*p* value
No. of samples	12	10	13	12	
Age (in years ± SE)	62.9 ± 2.2	76.2 ± 1.1	48 ± 3.0	61.7 ± 8.5	0.005
Male	6	5	5	7	0.052
Smokers	4	4	4	6	0.132
Diabetes	2	3	–	1	0.001
Hypertension	9	7	3	5	0.031
Hyperlipidemia	7	6	2	7	0.022
CAD	4	3	0	2	0.003
Aortic annulus (in cm)	_	–	3.1 ± 0.6	2.5 ± 0.5.	<0.001
AVA	>2.5	0.82 ± 0.2	2.8 ± 0.9	0.8 ± 0.2	–

All patients underwent a comprehensive echocardiographic assessment including, M-mode, two-dimensional and Color Doppler, conducted by a certified echo-cardiographer using commercially available ultrasound systems. All measurements were performed according to the American Society of Echocardiography recommendations. Aortic stenosis was defined as an aortic valve area (AVA) < 2.0 cm^2. Aortic valve calcification was assessed, and a calcium score of 1–4 was assigned by a single cardiologist based on the method described earlier.[18]

Subjects with any of the following conditions were excluded: patients with serum creatinine ≥1.5 mg/dl, premature menopause and/or osteoporosis, prior aortic valve surgery, rheumatic heart disease, endocarditis, active malignancy, chronic liver failure, calcium regulation disorders (known primary hyperparathyroidism, hyperthyroidism, and hypothyroidism), and chronic or acute inflammatory states (sepsis, autoimmune disease, and inflammatory bowel disease).

Tissue Preparation

Tissue and organ level analyses were performed at Center for Cardiovascular Simulation Biomechanical Experimental Laboratory. AV leaflets were randomly selected from non-, right, and left-coronary position (Fig. 1). BAV and TAV leaflets (acquired for SALS and histological analysis described next) were placed in 1× phosphate buffer saline (PBS), transported to CCS on ice and frozen at −80 °C for later use. At the time of testing, samples were quickly thawed, laid flat and fixed with 0.5% glutaraldehyde in PBS. Samples were then washed with PBS three times for 15 min each, and dehydrated in graded solutions of glycerol/PBS of 50, 75, 87 and 100% for an hour each.

Fiber Architecture Quantification

Small angle light scattering (SALS) system was used to determine the collagen fiber distributions in valve leaflets as previously described.[10] Briefly, 4 mW HeNe continuous non-polarized laser ($\lambda = 632.8$ nm) was passed through the tissue and scattered by the fibrous tissue onto a projection screen. The scattering pattern represents the angular distribution of collagen fibers within the light beam envelope. The preferred fiber orientation and orientation index (OI) were calculated from the pattern as previously described.[21] Scanning an entire leaflet with this procedure gives a fiber structure map of a single leaflet using 0.25 mm spaced points, which resulted in a very high density data (Figs. 2, 3, and 4).

Histology and Western Blotting

Histological analyses were performed by first embedding the samples in paraffin. Then, transverse sections were cut from both commissure and belly regions of the leaflets, with sections aligned such that the long axis was parallel to the preferred fiber direction. Section were stained with Picro Sirius Red and analyzed under polarized light to examine collagen fibers, or stained with Movat Pentachrome and analyzed with white field to examine extra cellular matrix (ECM) organization. In a different set of experiments at UPenn, histological analysis of all the tissues was performed by Hematoxylin and Eosin (H&E) and Modified Movat Pentachrome staining (for proteoglycans, elastin and collagen) according to the protocol of the Histology Laboratory of the UPenn School Of Medicine. Protein expression was carried out by using western blotting methods using specific antibodies.

Spline Mapping

Population-averaged microstructural maps for AV leaflets have not been obtained before. SALS experimental setup ("Fiber Architecture Quantification" section) gives the fiber structure for each individual leaflet. However, different leaflet samples had varied shapes. Therefore, the results from SALS could not be used directly to perform a statistical analysis in order to find average maps and variations among different AV groups. To solve this problem, fiber structure from

FIGURE 1. From left: *in vivo* non-calcified TAV, explanted calcified TAV, explanted non-calcified and calcified BAV leaflets. Calcification is usually coupled with strong inflammation and thickening.

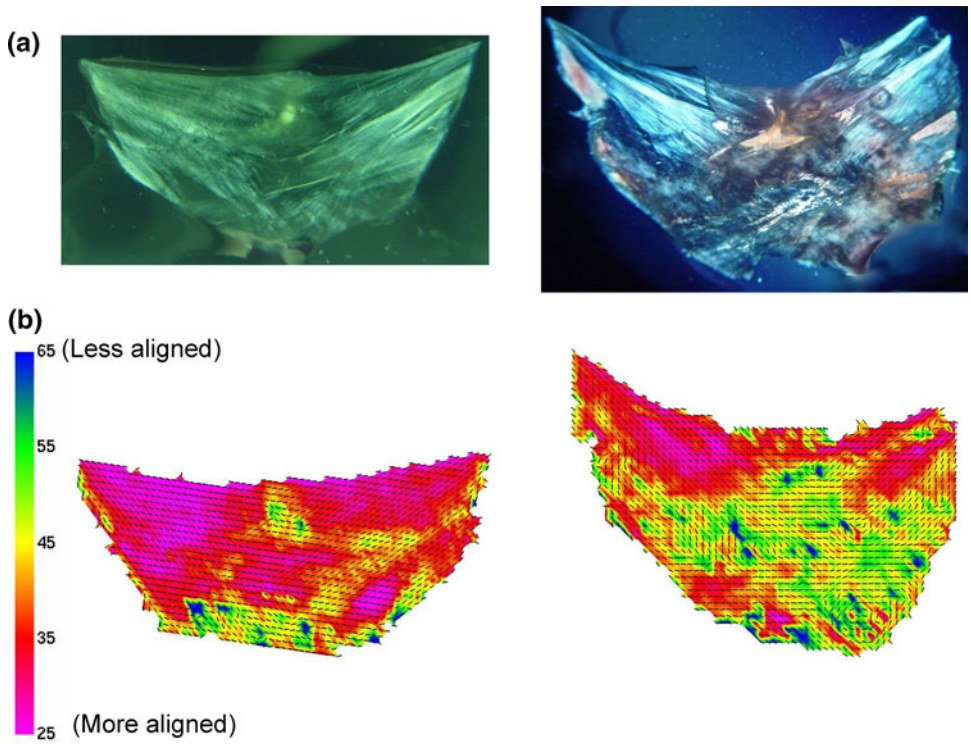

FIGURE 2. (a) Collagen architecture visible in TAV and BAV leaflets under polarized light and (b) quantified fiber architecture for representative TAV and BAV leaflets using SALS setup.

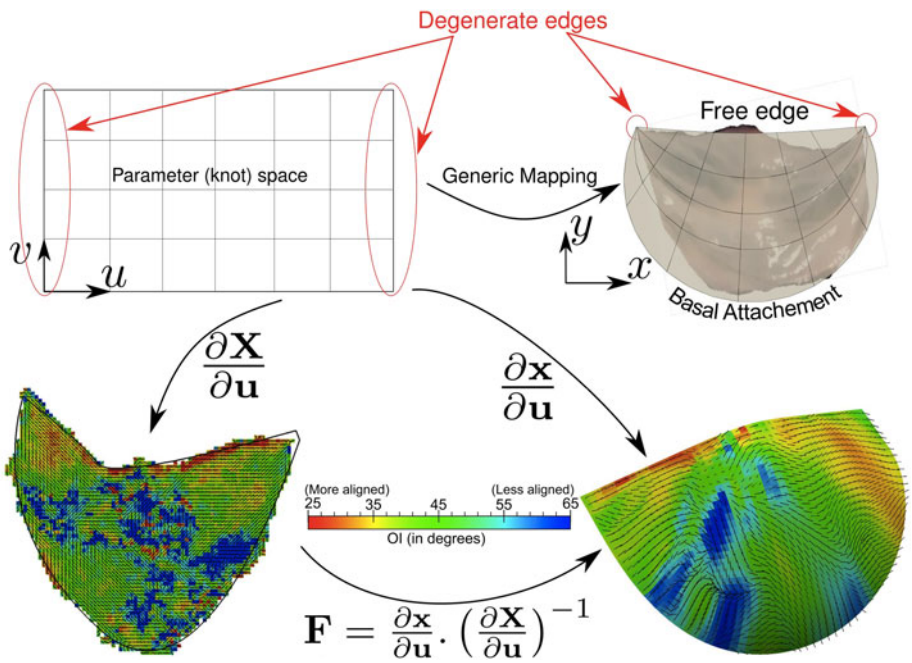

FIGURE 3. Method of spline flitting: Parameter space is specialized for the aortic valve by degenerating two of its edges. This gives a physical relation between the two configurations of the valve (2D and 3D) and a mapping in between them.

each sample had to be parametrically mapped to a common template structure. There are no standard methods available for such mapping. To this end, we developed a novel spline based mapping technique.

We fitted a spline surface to all sample data and calculated an equivalent fiber structure over the template through a mapping calculated *via* spline space. For such a mapping to be possible the parameter space

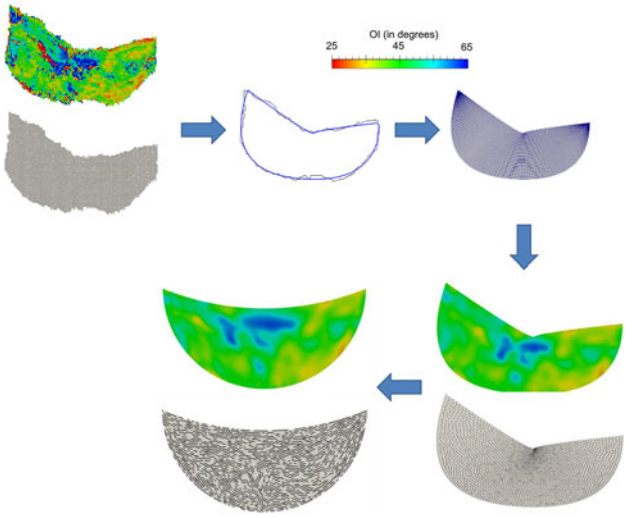

FIGURE 4. Steps in calculating the average microstructure. SALS experiment for each leaflet gives an individual microstructure map. These maps are fitted with spline curves and converted to surfaces. Then using the spline mapping, the SALS data is mapped onto a common template.

needed to be global and, thus, the spline surface was parameterized globally in the knot space with $(u, v) = [0,1] \times [0,1]$. Along with a global parameter space, splines were chosen because of their flexibility in setting desired continuity and ability to represent complex geometries with small number of control points. Usually, a spline surface has four edges whereas the aortic valve has only two (Fig. 1). Therefore, for mapping purposes two edges of the spline space ($u = 0$ and $u = 1$) were degenerated into two commissure points of the valve (top row in Fig. 3).

Directly fitting a surface to given point cloud data led to oscillations at the boundary. This was observed because of the lack of constraints on boundary control points. To avoid this problem, instead of direct surface fitting, a closed C^1-continuous spline curve with two C^0-continuous points (representing the commissures) was first fitted to the boundary. This closed curve was then converted into an open C^1-continuous spline surface (Fig. 4). Then the spline surface was fitted to the valve geometry while the boundary control points were kept fixed—thus eliminating the oscillation problem. For fitting, norm of the distance between the input points x_i and their projection on the spline surface x_i^p was minimized to find the control points C_j:

$$\mathbb{F}(x_i) = \min_{C_j} \sum_i |x_i - x_i^p|^2 \equiv \min_{C_j} \sum_i \left| x_i - \sum_j N_j(u_i^p, v_i^p) C_j \right|^2 \equiv \min |x - AC|^2, \tag{1}$$

where $\mathbf{C}$ is a vector of the control points C_j and $\mathbf{A}$ is the matrix of shape functions with the (i, j)th term $= N_j(u_i^p, v_i^p)$. Details of splines can be found in any standard computer aided design book, for example Bartels *et al.*[3] Briefly, in one dimension, the spline shape functions were calculated starting from zeroth order shape functions (which are step functions) recursively as follows

$$N_{i,0}(u) = \begin{cases} 1 & \text{if } u_i \le u < u_{i+1} \\ 0 & \text{otherwise} \end{cases},$$
$$N_{i,p}(u) = \frac{u - u_i}{u_{i+p} - u_i} N_{i,p-1}(u) + \frac{u_{i+p+1} - u}{u_{i+p+1} - u_{i+1}} N_{i+1,p-1}(u) \tag{2}$$

where $N_{i,p}(u)$ is the p-order spline shape function at u (C^{p-1}-continuous unless knots are repeated) and u_i is the ith component in the knot vector. For two dimensions, the shape functions were constructed from 2 one-dimensional shape functions (one in direction u and other in v) by an outer product $N_{(i\times j)}(u, v) = N_i(u) \times N_j(v)$. The minimization problem (Eq. (1)) can be easily shown to be equivalent to solving a linear system $\mathbf{C} = (\mathbf{A}^T\mathbf{A})^{-1}\ \mathbf{A}^T\mathbf{x}$ when the projection coordinates (u_i^p, v_i^p) are known. Assuming that a close guess of the final solution—the control points—was known from previous iteration, the point on spline, (u_i^p, v_i^p) closest to the point x_i was found by a projection operator. As the closest (projection) point should make a normal to the spline, it was calculated by solving the orthogonality condition $(x_i - x_i^p) \cdot \frac{dx_i^p}{du} = 0$ using Newton's method (Fig. 5a). This projection operation becomes a little more involved in the case of open surface fitting because the points close to boundary may not have a perpendicular projection on the surface. In such a case, the solution was restricted to the boundary and then solved again (Fig. 5b).

The spline curve was initialized with four control points initialized manually and refined until desired accuracy was obtained (RMSD $= \frac{1}{n}\mathbb{F}(x_i) < 0.25$ mm the resolution of SALS device, n being the number of input points). To convert the spline curve to a surface, it should be noted that the number of control points and knot intervals were required to be same in the two parts of the curve. If this condition was satisfied, the two C^1-continuous parts were split and the second part was reversed. Then a knot vector in v direction was constructed as per the desired continuity (C^1 here) and the control points in between two edges were interpolated linearly to obtain the initial guess to spline surface (Fig. 4). For SALS data, this spline surface was the final resulting fit. However, for data from 3D imaging, e.g., ultrasound, the interpolated surface showed some error in the interior (2 examples shown in

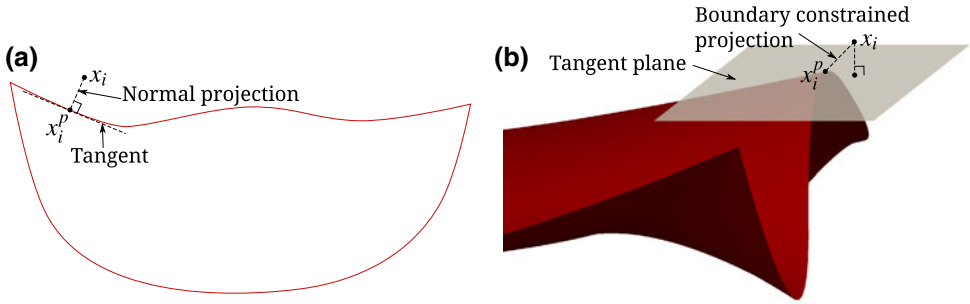

FIGURE 5. (a) The projection or closest point is orthogonal to the curve/surface and is calculated by solving the normality condition using Newton's method. (b) In case of surface, some boundary points may not satisfy this condition fully and have to be constrained on the boundary.

Fig. 6). Therefore, the same minimization procedure (Eq. (1)) was applied with the interpolated surface being our initial guess. During this minimization, the boundary of surface was kept fixed since it had already been fitted to the data. The procedure gave us new control points and thus the final spline surface fitted to the given point cloud with error smaller than the imaging resolution.

In order to obtain gross geometric parameters at the organ level, the spline surfaces fitted onto the SALS spatial positional data were measured to obtain distance between commissure points, lengths of free edge and basal attachment, and surface area for each case. Means and standard deviations were calculated for each geometric parameter. A template valve shape was constructed using the average geometric lengths and making an assumption that both edges of the valve were circular arcs. Then, a spline surface was fitted to this template using the same procedure.

For mapping the fiber structure data from each of the explanted leaflets onto the average common template, corresponding points in the two configurations (explanted and average) were obtained through the knot space (same u and v, Fig. 3). So the OI (scalar) was mapped simply as $\mathrm{OI}^X(u,v) = \mathrm{OI}^x(u,v)$. For the fiber direction, the mapping from knot space (u) to any spline (X) is $\frac{\partial X}{\partial u} = \sum_i \frac{\partial N_i}{\partial u} C_i$, which can be calculated simply from the control points and first derivatives of the shape functions. If the mapping between knot space and spline fit onto SALS data is $\frac{\partial X}{\partial u}$ and that between the knot space and spline fit onto 3D geometry or average template is $\frac{\partial x}{\partial u}$, then the mapping from SALS spline to 3D geometry/average template spline is $\mathbf{F} = \frac{\partial x}{\partial u}\left(\frac{\partial X}{\partial u}\right)^{-1}$ (Fig. 3). This deformation map F was used for calculating equivalent preferred fiber directions on the template geometry. Further the data was smoothed using a Gaussian kernel with a standard deviation equal to three times the resolution of SALS setup. Once the fiber structure from each leaflet was mapped onto the common template, statistical analyses were performed to calculate the average microstructure and variability among the tested human population (details of statistical analyses are provided in "Statistical Analysis" section).

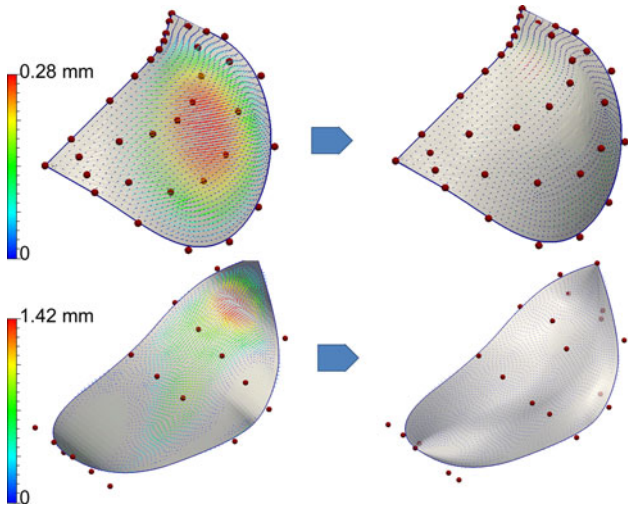

FIGURE 6. Spline fitting to a 3D point cloud includes an extra step after the conversion of spline curve into a surface: the interior control points are fitted to minimize the error and obtain the final spline representation (color represents the projection error).

Validation of the Mapping Procedure

To validate this mapping procedure two sets of existing data were used. We utilized 9 markers applied on a fixed porcine bioprosthetic heart valve and then imaged using magnetic resonance imaging (MRI) in 3D and using SALS in 2D.[25] To use this data for validation, both 2D and 3D images were hand-digitized to get the marker positions x^{2D} and x^{3D} respectively. Spline surfaces were fit onto both 2D and 3D marker configurations using the method described in "Spline Mapping" section. Then the marker positions from 2D were mapped onto the 3D spline surface [such

that they have the same knot space coordinates (u, v)] to obtain the mapped marker position in 3D x^{3D}_{mapped}. This was compared to the actual marker positions x^{3D} and mapping error was calculated. For second validation, data from a pericardial bioprosthetic heart valve placed in a mock physiological flow loop and imaged using biplane X-ray was used.[27] Two farthest apart frames of valve were used as the two configurations—both in 3D—to quantify the error for mapping between two 3D configurations. The markers from configuration 1 (x^1) were mapped to the other configuration 2 (x^2_{mapped}) and compared with the actual marker positions (x^2). The error was quantified as the maximum and mean distance between actual and mapped marker positions.

Isolations of Aortic Valve Interstitial Cells

In parallel to the studies of fiber architecture, we also sought to study the differences between VICs of TAV and BAV, and their effect on CAVD separated from the microstructural effects. To accomplish this experiments were performed on isolated cells *in vitro*. Isolation of aortic VICs was performed using a modification of the method described by Sainger *et al*.[22] Cells were cultured and grown in advanced Dulbecco's modified Eagle's medium (DMEM) and used for experiment between the second and fifth passage. Characterization of VICs was carried out using smooth muscle actin (SMA), vimentin and glyceraldehyde 3-phosphate dehydrogenase (GAPDH) (loading control) expression in the VICs from all the four groups.

In Vitro Calcification

In vitro calcification assay was performed using VICs isolated from non-calcified BAV and TAV aortic valves. Cells were cultured in advanced DMEM containing P/S, L-glutamine and 10% Fetal Bovine Serum (FBS), until 70–80% confluent. Growth medium was replaced by calcification media (α-MEM containing 3 mM phosphate buffer) in all wells except the control. Medium was replaced every 2 days. At day 9, VICs were incubated overnight in 0.6 NHCl at 4 °C. Calcium was estimated using the calcium assay reagent (Biovision, Mountain View, CA). Amount of total calcium was expressed as mg of calcium/mL of medium.

Statistical Analysis

Summary statistics on gross geometric parameters were calculated based on 23 TAV (9 non-calcified and 14 calcified) leaflets and 11 BAV (8 non-calcified and 3 calcified) leaflets (a subset of all the samples with demographics is shown in Table 1). Basic geometric features (distance between commissure points, length of basal attachment and free edge, and leaflet area) were calculated for each sample using spline surface fits to SALS data. Means and variability (in terms of 99% bootstrap confidence intervals because the distribution cannot be assumed to be normal and sample size is small) were calculated separately for TAV and BAV groups. Non-parametric Wilcoxon tests were performed to determine the statistical significance of the differences between the two groups with $p < 0.05$ defined as the threshold.

For the collagen architecture mapping, only non-calcified leaflets were used as the focus was on early disease stage analysis. Nine non-calcified TAV leaflets and five non-calcified BAV leaflets were used to determine the fiber structure using SALS. For each leaflet the fiber structure was mapped onto the common template using the spline mapping technique ("Spline Mapping" section). Further, the average (mean) microstructure and standard deviation were calculated using package R (http://www.r-project.org/). Sample mean and standard deviation were computed for the OI, however means and standard deviations for circular data[12] (with a periodicity of 180 degrees) were computed for the fiber direction. To test for differences between TAV and BAV microstructure, a non-parametric Wilcoxon test was performed to calculate the T-statistic for each test point on the valve. The differences were seen in a relative sense since no correction was made for multiplicity in the p values.

To determine the degree of *spatial correlation*, i.e., how much the fiber architecture at one point of the valve correlates with other points of the valve, a Moran's I test was used.[13,14] Briefly, the test uses the data and spatial distances between test points. It provides a scalar index between −1 and 1 with a certainty in terms of standard error. An index value of −1 indicates perfect negative correlation and 1 indicates perfect positive correlation, whereas an autocorrelation of 0 indicates that all the results obtained are independent of each other. In addition, to clarify spatial correlations, a simple region analysis was performed. Here, for region analysis, group of points located in 10 square regions were selected. Data over each region was represented in terms of mean and variation (99% bootstrap confidence intervals) among all the samples within that region.

RESULTS

Cellular Level

H&E and modified Movat's Pentachrome staining were used to analyze calcified and non-calcified aortic valve leaflets from BAV and TAV patients. The results

from histological analysis show side specific dysfunction of the fibrosa in both BAV and TAV parallel with proteoglycan and calcium accumulation (Fig. 7a). VIC were then isolated and analyzed for expression of SMA and Vimentin.[4,15] The results from western blotting indicate that VICs maintain overexpression of SMA (Figs. 7b and 7c), suggesting phenotypic stability even in the isolated state. We therefore tested the ability of isolated VICs from non-calcified BAV and TAV patients to undergo *in vitro* calcification. Interestingly, when stimulated to inorganic phosphate in an *in vitro* calcification assay VICs from BAV and TAV show similar pattern of calcium accumulation (Fig. 7d).

Tissue Level

Histological analysis on TAV and BAV leaflet sections shows interesting results (Fig. 8). TAV has a very organized structure with most of the fibers aligned, even across various layers. However in the BAV case,

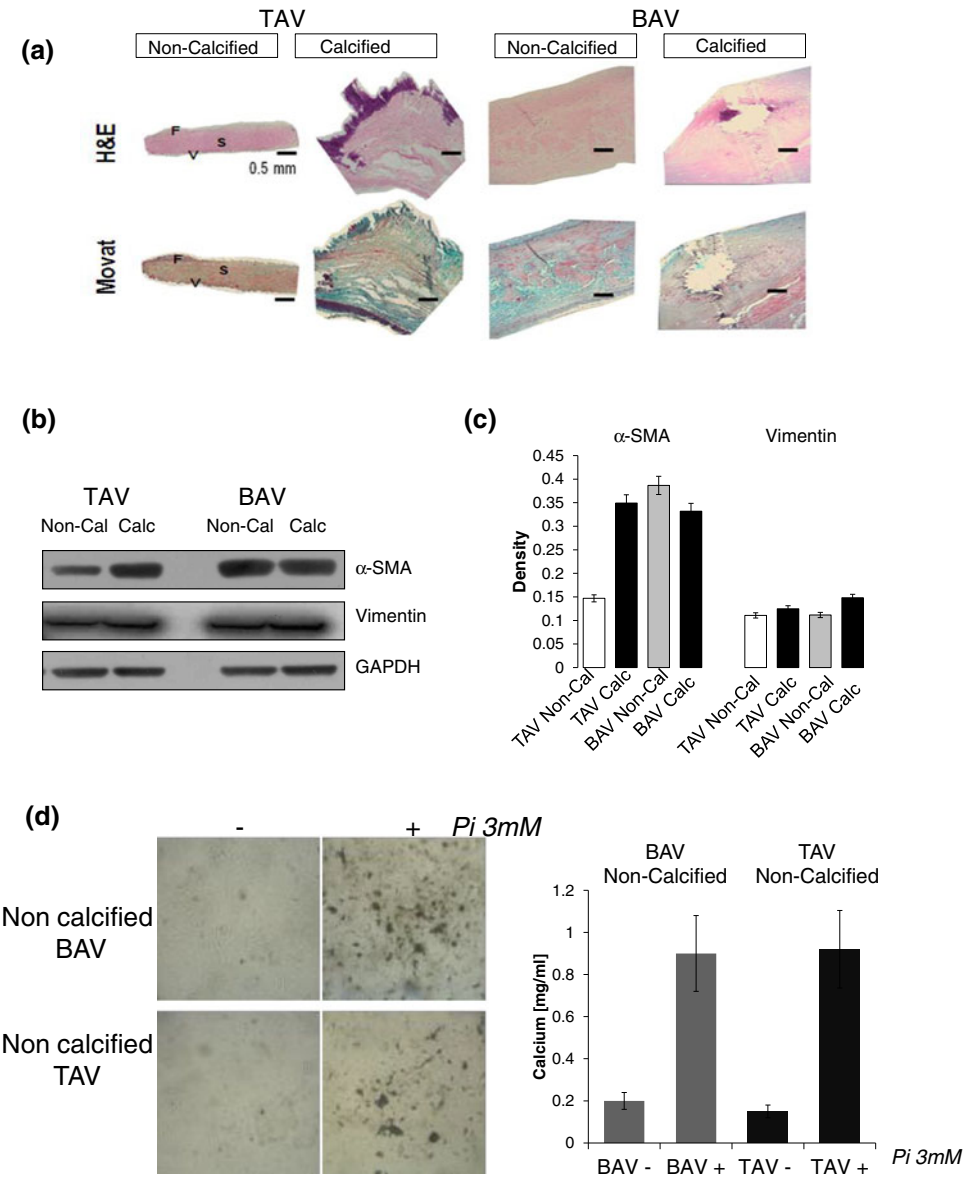

FIGURE 7. (a) Analysis of aortic valve (AV) microstructure, ECM organization in representative tissues from non calcified and calcified tricuspid (TAV) and BAV—H&E and Movat staining in the AV tissues; ECM components are distinguished as proteoglycan (bluish green), collagen (yellow), and elastin (dark violet); VIC nuclei are stained dark red; F, S and V represent fibrosa, spongiosa and ventricularis respectively. (b, c) Characterization of VICs isolated from AV tissues—western blot and bar graph showing SMA and vimentin expression in AV VICs, GAPDH serves as loading control. (d) *In vitro* calcification assay—images are representative of calcification assay performed on VICs isolated from non-calcified TAV and BAV using 3 mM Pi. Calcium was quantified by colorimetric assay and represented as calcium mg/mL.

fibers have a very disordered arrangement indicating that it is a layer level anomaly (Fig. 8a). Normally, the elastin is present in the ventricularis layer as observed in the TAV case. However, in one BAV case, the layers are mixed and a big block of elastin is found in the middle of the tissue (Fig. 8b).

Organ Level

All of the mean geometric parameters for TAV and BAV groups show significant differences (Fig. 9). Clearly, the BAVs have larger leaflets compared to TAV on an average. Also, their shape is fairly consistent, however less consistent than the TAV leaflet shape. Assuming that edges of the average shape are circular arcs, average shapes are drawn and overlapped for the two cases clearly showing the differences in BAV and TAV.

The collagen architecture is clearly visible when two representative valves (non-calcified TAV and BAV) are observed under polarized light (top row Fig. 2). We can see that overall the fibers go in the circumferential

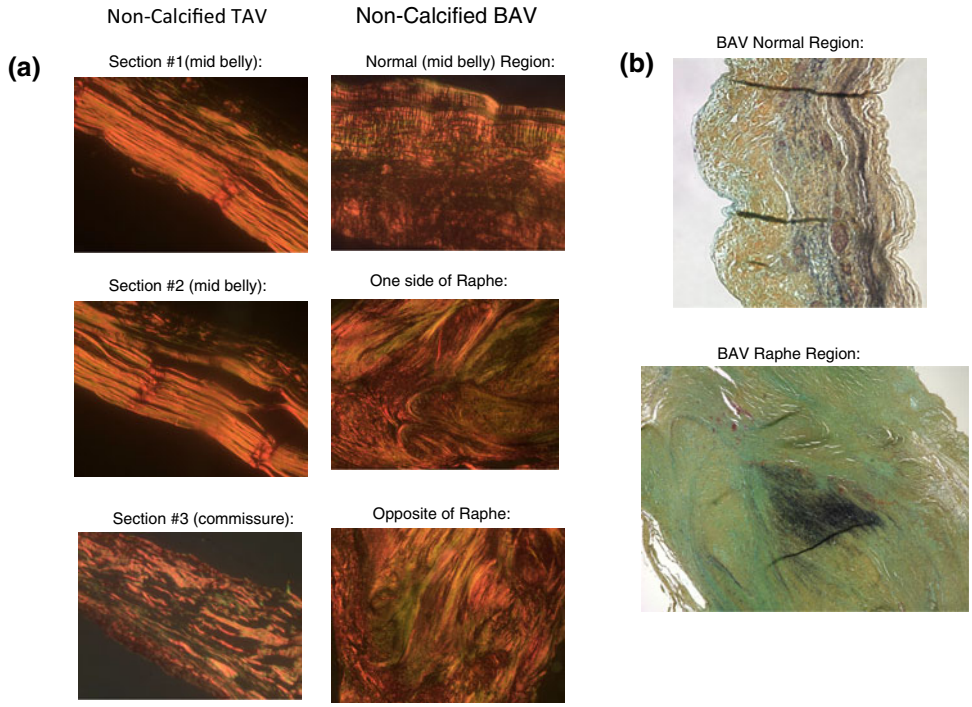

FIGURE 8. (a) Representative layer arrangement from histology shows organized and aligned layers in the TAV but disorganized ones in BAV especially around the raphe. (b) A packet of elastin is seen in the BAV raphe region.

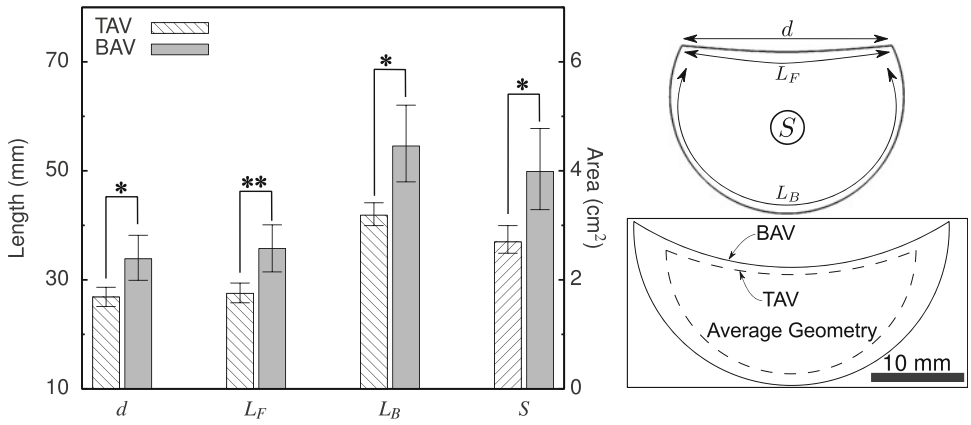

FIGURE 9. (a) Basic geometric parameters—distance between commissure points *d*, length of the free edge L_F, length of the basal attachment L_B and area *S*, were calculated for all the explants and divided into two groups, TAV and BAV, for statistical analysis. There were statistically significant differences in all four parameters, (b) average geometry of TAV and BAV using these parameters (*$p < 0.01$ and **$p < 0.005$).

direction. However, the arrangement looks somewhat less organized in the belly region, which can also be confirmed using quantified fiber arrangement from SALS (bottom row Fig. 2). To quantitatively determine the population averaged microstructure and differences between TAV and BAV, spline mapping technique gives the equivalent architecture maps for each valve.

The error of mapping for both validation cases was within an acceptable range. Specifically, for the case of marker positions being mapped between two frames in a flow loop, the maximum error was ~1.5 mm, with a mean error for all the markers of 0.58 mm and the error for the interior marker was <0.7 mm. The errors were thus smaller than the resolution of imaging modality, therefore validating the technique for mapping microstructure. The error was observed to become larger when derivatives of the mapping, i.e., the strain between two configurations were calculated. This accuracy of the method might be improved by adding regularization term in the function (equation 1). This will be explored in future studies, so that it allows us to calculate the strain accurately as well.

The averaged microstructural maps for TAV and BAV on 2D template show interesting trends (Fig. 10a). These average maps were mapped onto 3D *in vivo* geometry from ultrasound for both TAV and BAV for visualization (Fig. 11). For every leaflet the Moran's I spatial correlation index lies between 0.15 and 0.25 (mean $\approx$ 0.18 and standard deviation $\approx$ 0.04 within each group) for both TAV and BAV with high certainty (standard error for each test 10^{-3}). This indicates that the OI for all individual samples are (weakly) positively correlated spatially and thus Bonferroni correction would be too conservative here. The p values for differences in the distributions of microstructure in TAV and BAV cases over the 2D template indicate that the microstructure is most different in the belly region of valve, but only in terms of OI (Fig. 10b). In the terms of mean fiber directions, p values are mostly > 0.2, therefore, the mean fiber directions are not significantly different in two cases. This indicates that the fibers on an average are going in the same direction for both TAV and BAV. However, they are much less aligned around the belly region of the BAV leaflets. Performing a region wise analysis to minimize the effects of spatial autocorrelation shows the consistency in OI for both TAV and BAV cases (Fig. 10c). Further, in regions A, B, C, D and G the OI for TAV case is clearly larger than the BAV case.

DISCUSSION

Challenges in BAV Research

In general, BAV patients face a higher risk of developing valve related diseases. It is known that, irrespective of the exact valvular anatomical anomaly, all BAVs have altered mechanical stress distribution and hemodynamics, that ultimately may be linked to accelerated aortic stenosis (AS), aortic insufficiency (AI), endocarditis, ascending aortic aneurysm with or without associated AI and aortic dissection.[6,7,11,24] The underlying pathological mechanisms should involve VICs, which exhibit profound sensitivity to mechanical cues—selectively elaborating osteogenic potential under the correct mechanical environment.[15,29]

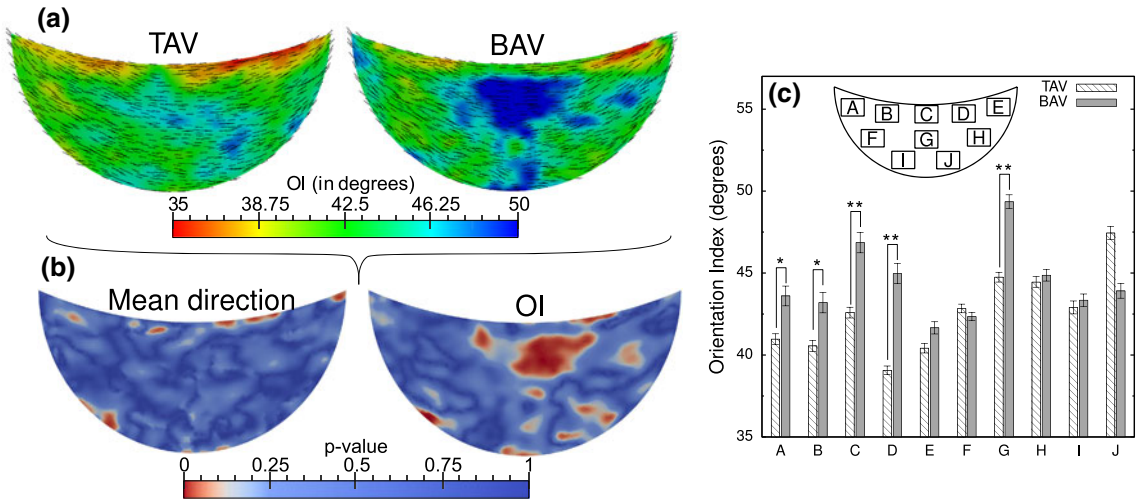

FIGURE 10. (a) Explants from human sub-population TAV and BAV were used to determine the microstructure and then averaged to obtain the average microstructure maps. (b) Statistical analysis on mean fiber directions (left) and OI (right) shows important differences in the belly region for OI but the mean fiber directions are similar in two cases. (c) Summary statistics based on regions shows consistency in the structure of the leaflets from both groups (*$p<0.01$ and **$p<0.005$).

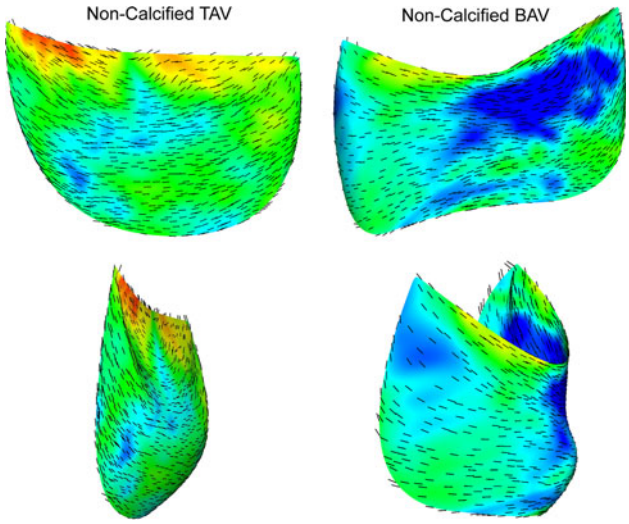

FIGURE 11. Using the 3D spline mapping, average microstructure was mapped onto *in vivo* geometries for TAV and BAV respectively (obtained from hand-digitized ultrasound imaging of human aortic valve at mid-systole point of cardiac cycle).

However, very little is known about the underlying mechanisms or even the microstructural differences between the TAV and pathological BAV at different scales, and how these differences might contribute to accelerated calcification. Therefore, in the current study we hypothesized that the abnormalities in the structure of BAV, from organ level to the tissue to the interstitial cells, may contribute to the CAVD and AS. The significant inflammation in the later stages of CAVD (Fig. 1) makes detailed and meaningful microstructural studies almost impossible. Also, an early identification of patients who are at the greatest risk of developing AS would be of great clinical value.[28] Therefore, here we focused on early disease stage leaflets and studied the differences that might contribute to the accelerated disease development in patients.

Overall Findings

At the cellular level, we found that the VICs when isolated from both types of valve respond to calcification stimulus in a similar fashion. *In vitro* calcification assays was performed using 3 mM inorganic phosphate on isolated VIC at passage 2–4. Here we report that VIC isolated from BAV and TAV patients show similar pattern of calcium accumulation. These data are not intended to prove a phenotypic equivalence between VIC from different patients, but rather to demonstrate the equal intrinsic capacity of BAV and TAV isolated VIC to respond to *in vitro* calcification stimuli. In Fig. 7 and Supplemental Fig. 1 we show a similar expression pattern of several markers of VIC activation for calcified and non-calcified BAV and TAV-derived cells. Although a deeper phenotypic analysis of the phenotypic variation of BAV-derived VIC is necessary, our preliminary data suggest that BAV cells are not inherently abnormal, and suggests the local and mechanical factors could be responsible for the abnormal function of these cells *in vivo*.

At the tissue level, we quantified the collagen fiber architecture to obtain population-based trends using a spline based mapping technique (Figs. 10 and 11). As our emphasis was on early disease stage analysis, we used non-calcified valve leaflets. Interestingly, we did not find significant differences in the mean fiber direction in two cases which suggests that on a coarse scale, the fibers are still running predominantly along the circumferential direction, however the fibers are less aligned in the belly area, and may have an isotropic structural response. Histologically, the normal AV leaflets layers were found to be well organized and distinct (Fig. 8). However, for bicuspid leaflets we demonstrated a disorganized structure indicating that the layer structures appear intermingled and indistinct. The greater thickness found for the BAV leaflets around the raphe region was a direct result of the residual, largely disorganized tissue that composes the Raphe. As a result, this region's collagen fiber architecture becomes less aligned, as found in our population averaged fiber maps (Fig. 10). For this region only we can say that thickness of the leaflet and disorganization of collagen fibers may thus be correlated. However, no measurements were made directly on the thickness of leaflets.

At the organ level, looking at gross geometric features, the average BAV leaflets are significantly larger but have similar semilunar shape, albeit slightly more elongated (Fig. 9). This is not surprising as two BAV leaflets cover the same area as three of the normal AV leaflets do. We noticed these differences in all the geometric factors and also quantified variation in the leaflet shape. These findings are important to determine how patient specific we need to make our model geometries to obtain physiologically accurate results.

Future Directions

Simulation of normal and pathological valves requires the correct input data for the simulations to be meaningful and realistic. In fact, a major goal of the present work was to provide such data (structure in this case), which is known to play such an important role in valve mechanics.[19] The fact that we found, much to our surprise, that explanted BAV have a good degree of structural regularity will be critical in modeling work, which we are currently planning. The average maps calculated here can play a critical role in

modeling efforts where microstructure of a human patient is not known, but instead represented from patient population trends. More importantly, comparing the two cases we saw important differences in the OI around the belly region of leaflets. This is the region where leaflets fuse together during heart development and also shows a highly disorganized structure in histological analysis (Fig. 8). Further, the novel spline mapping technique developed here is useful in other applications as well. For example, it has been used for estimating the *in vivo* pre-strain,[1] which is critical information for many modeling studies including inverse models for evaluating mechanical properties of valve leaflets from *in vivo* imaging. This will be a subject of future research.

In the present study, the focus was on finding structural trends in pre-diseased valve tissue, as a first step toward developing an understanding of the structural features of the BAV, as such features are known to play an important role in valve mechanics.[19] The relation between fiber architecture, as well as organ level geometry and the onset/progression of calcification remains unknown, and is well beyond the scope of present study. It can be speculated that the disorganized layers and thicker leaflet lead to altered local cell micromechanical environment. The lower orientation around belly area in BAV leaflets may lead to a more isotropic mechanical response and altered mechanical stress state. Mechanical forces have been shown to activate the biomineralization and calcification of VICs,[15] thus suggesting a relation between calcification and the local mechanical stress environment. Regarding the inception site of calcification, in explanted bioprosthetic heart valves, it has been previously shown that calcification and structural damage are not spatially correlated.[20] However, no such studies have been done on BAV to the authors' knowledge. More detailed analysis of this relation between calcification potential, BAV leaflet structure, and surface shear forces, will need to be explored in future studies.

Limitations

Although we found consistent patterns in the present population, the sample size was not sufficient to reveal larger population trends. Moreover, here we analyzed only one BAV group. With larger sample size, it would be interesting to evaluate structural differences between different configurations of the BAV anomaly, which can range from a single to four leaflets. We thus should consider the current results as initial indicators that will help guide future research and motivate more focus on the microstructural effects in BAV disease development. There are also different possible factors that may contribute to the CAVD development, e.g., the effect of shear stresses due to changes in blood flow on endothelium and calcification pathway.[2] In the current study, we focused only on the microstructural effects. Combined effects of the differences in microstructure as well as shear stresses using fluid–structure interaction models will need to be investigated.

Summary

In conclusion, we found statistically different and consistent regional structures between the normal and bicuspid valves. The regularity in the observed microstructure was a surprising finding, especially for the pathological BAV leaflets and is an essential cornerstone of any predictive mathematical models of valve disease. In contrast, we determined that isolated VICs from BAV leaflets show the same *in vitro* calcification pathways as those from the normal AV leaflets. This result suggests the VICs are not intrinsically different when isolated, and that external features, such as abnormal microstructure and altered flow may be the primary contributors in the accelerated calcification experienced by BAV patients.

ELECTRONIC SUPPLEMENTARY MATERIAL

The online version of this article (doi:10.1007/s10439-014-0973-0) contains supplementary material, which is available to authorized users.

ACKNOWLEDGMENTS

This work was supported by the following sources—National Institute of Health (grant number grant numbers HL63954, HL103723 and HL73021 to R.C.G. and J.H.G.) and Moncrief Chair funds (M.S.S.). Help from Vanessa Aguilar in carrying out several of the experiments is greatly appreciated. American Heart Association Postdoctoral Fellowship Award 14POST18720037 to A.A.

CONFLICT OF INTEREST

None declared.

REFERENCES

[1]Aggarwal, A., V. S. Aguilar, C.-H. Lee, G. Ferrari, J. H. Gorman, R. C. Gorman, and M. S. Sacks. Functional Imaging and Modeling of the Heart, Springer, 2013, pp. 141–149.

[2]Balachandran, K., P. Sucosky, and A. P. Yoganathan. Hemodynamics and mechanobiology of aortic valve inflammation and calcification. *Int. J. Inflam.* 2011:263870, 2011. doi:10.4061/2011/263870.

[3]Bartels, R. H., J. C. Beatty, and B. A. Barsky. An Introduction to Splines for Use in Computer Graphics and Geometric Modeling. Los Altos, CA: Morgan Kaufmann, 1987.

[4]Branchetti, E., R. Sainger, P. Poggio, J. B. Grau, J. Patterson-Fortin, J. E. Bavaria, M. Chorny, E. Lai, R. C. Gorman, R. J. Levy, and G. Ferrari. Antioxidant enzymes reduce DNA damage and early activation of valvular interstitial cells in aortic valve sclerosis. *Arterioscler. Thromb. Vasc. Biol.* 33(2):e66–e74, 2013.

[5]De Sa, M. P., E. S. Bastos, and H. Murad. Bicuspid aortic valve: theoretical and clinical aspects of concomitant ascending aorta replacement. *Rev. Bras. Cir. Cardiovasc.* 24(2):218–224, 2009.

[6]Evangelista, A. Bicuspid aortic valve and aortic root disease. *Curr. Cardiol. Rep.* 13(3):234–241, 2011.

[7]Fedak, P. W., S. Verma, T. E. David, R. L. Leask, R. D. Weisel, and J. Butany. Clinical and pathophysiological implications of a bicuspid aortic valve. *Circulation* 106:900–904, 2002.

[8]Friedman, T., A. Mani, and J. A. Elefteriades. Bicuspid aortic valve: clinical approach and scientific review of a common clinical entity. *Expert Rev. Cardiovasc. Ther.* 6(2):235–248, 2008.

[9]Garg, V. Molecular genetics of aortic valve disease. *Curr. Opin. Cardiol.* 21(3):180–184, 2006.

[10]Joyce, E. M., J. Liao, F. J. Schoen, J. E. Mayer, Jr., and M. S. Sacks. Functional collagen fiber architecture of the pulmonary heart valve cusp. *Ann. Thorac. Surg.* 87(4):1240–1249, 2009.

[11]Lewin, M. B., and C. M. Otto. The bicuspid aortic valve: adverse outcomes from infancy to old age. *Circulation* 111(7):832–834, 2005.

[12]Mardia, K. V. Statistics of Directional Data. New York: Academic Press, 1972.

[13]Moran, P. A. Notes on continuous stochastic phenomena. *Biometrika* 37(1–2):17–23, 1950.

[14]Paradis, E., J. Claude, and K. Strimmer. APE: Analyses of Phylogenetics and Evolution in R language. *Bioinformatics* 20(2):289–290, 2004.

[15]Poggio, P., R. Sainger, E. Branchetti, J. B. Grau, E. K. Lai, R. C. Gorman, M. S. Sacks, A. Parolari, J. E. Bavaria, and G. Ferrari. Noggin attenuates the osteogenic activation of human valve interstitial cells in aortic valve sclerosis. *Cardiovasc. Res.* 98(3):402–410, 2013.

[16]Roberts, W. C., and J. M. Ko. Frequency by decades of unicuspid, bicuspid, and tricuspid aortic valves in adults having isolated aortic valve replacement for aortic stenosis, with or without associated aortic regurgitation. *Circulation* 111(7):920–925, 2005.

[17]Robicsek, F., M. J. Thubrikar, J. W. Cook, and B. Fowler. The congenitally bicuspid aortic valve: how does it function? Why does it fail? *Ann. Thorac. Surg.* 77(1):177–185, 2004.

[18]Rosenhek, R., T. Binder, G. Porenta, I. Lang, G. Christ, M. Schemper, G. Maurer, and H. Baumgartner. Predictors of outcome in severe, asymptomatic aortic stenosis. *N. Engl. J. Med.* 343(9):611–617, 2000.

[19]Sacks, M. S., W. D. Merryman, and D. E. Schmidt. On the biomechanics of heart valve function. *J. Biomech.* 42(12):1804–1824, 2009.

[20]Sacks, M. S., and F. J. Schoen. Collagen fiber disruption occurs independent of calcification in clinically explanted bioprosthetic heart valves. *J. Biomed. Mater. Res.* 62(3):359–371, 2002.

[21]Sacks, M. S., D. B. Smith, and E. D. Hiester. A small angle light scattering device for planar connective tissue microstructural analysis. *Ann. Biomed. Eng.* 25(4):678–689, 1997.

[22]Sainger, R., J. B. Grau, E. Branchetti, P. Poggio, W. F. Seefried, B. C. Field, M. A. Acker, R. C. Gorman, J. H. Gorman, 3rd, C. W. Hargrove, 3rd, J. E. Bavaria, and G. Ferrari. Human myxomatous mitral valve prolapse: role of bone morphogenetic protein 4 in valvular interstitial cell activation. *J. Cell. Physiol.* 227(6):2595–2604, 2012.

[23]Schaefer, B. M., M. B. Lewin, K. K. Stout, E. Gill, A. Prueitt, P. H. Byers, and C. M. Otto. The bicuspid aortic valve: an integrated phenotypic classification of leaflet morphology and aortic root shape. *Heart* 94(12):1634–1638, 2008.

[24]Siu, S. C., and C. K. Silversides. Bicuspid aortic valve disease. *J. Am. Coll. Cardiol.* 55(25):2789–2800, 2010.

[25]Smith, D. B., M. S. Sacks, P. M. Pattany, and R. Schroeder. High-resolution magnetic resonance imaging to characterize the geometry of fatigued porcine bioprosthetic heart valves. *J. Heart Valve Dis.* 6(4):424–432, 1997.

[26]Sun, L., S. Chandra, and P. Sucosky. Ex vivo evidence for the contribution of hemodynamic shear stress abnormalities to the early pathogenesis of calcific bicuspid aortic valve disease. *PLoS ONE* 7:e48843, 2012. doi:10.1371/journal.pone.0048843.

[27]Thornton, M. High Speed Dynamic, 3-D Surface Imaging. London, ON: Electrical Engineering, University of Western Ontario, 1996.

[28]Towler, D. A. Molecular and cellular aspects of calcific aortic valve disease. *Circ. Res.* 113:198–208, 2013. doi:10.1161/CIRCRESAHA.113.300155.

[29]Yip, C. Y., and C. A. Simmons. The aortic valve microenvironment and its role in calcific aortic valve disease. *Cardiovasc. Pathol.* 20(3):177–182, 2011.